CHAPTER *8*

IMAGE RECONSTRUCTION

Medical imaging modalities with instrumentation have been described in Chapters 4–7. As imaging instrumentation and computing capabilities evolved for data acquisition in two and three dimensions, computerized algorithms for multidimensional image reconstruction were developed. The historical perspective of image reconstruction algorithms started with J. Radon (1), who laid the mathematical foundation of image reconstruction from projections in his classic paper that was published in 1917. But the implementation of the Radon transform for reconstructing medical images was only realized in the 1960s. In 1972, G.N. Hounsfield developed the first commercial X-ray computed tomography (X-ray CT) scanner that used a computerized image reconstruction algorithm based on the Radon transform. G.N. Hounsfield and A.M. Cormack jointly received the 1979 Nobel prize for their contributions to the development of CT for radiological applications (2–4).

The classic image reconstruction from projection method based on the Radon transform is popularly known as the backprojection method. The backprojection method has been modified by a number of investigators to incorporate specific data collection schemes and to improve the quality of reconstructed images. Fourier transform and iterative series expansion-based methods have been developed for reconstructing images from projections. With the fast-growing developments in computer technology, advanced image reconstruction algorithms using statistical and estimation methods were developed and implemented for several medical imaging modalities. Recently, wavelet transform and other multiresolution signal processing methods have been applied in multidimensional image reconstruction.

Image reconstruction algorithms use the raw data collected from the imaging scanner to produce images that can provide information about internal physiological structures and associated properties. Reconstructing images from raw data is similar to solving a large number of simultaneous equations with unknown variables as it is mathematically proven that the number of simultaneous equations (analogous to measurements) should be at least equal to the number of unknown variables for determining a unique solution. In medical imaging, images are required to be reconstructed with high spatial resolution from the limited raw data. The number of measurements in the data collected during the scanning of a patient is much smaller than the number of unknown variables (pixels in two-dimensional [2-D] space; voxels in three-dimensional [3-D] space) to be solved for image reconstruction. As is evident from the imaging instrumentation discussed in Chapters 4–7, the measurements in

the data acquisition process are limited because of the limitations of detector subsystems, imaging geometry, physics of imaging, and patient scanning time. Furthermore, the measurements are degraded due to noise, scattering, geometrical occlusions, and errors in the data acquisition process. Thus, image reconstruction is an ill-posed problem as it is not possible to determine a unique solution from such an underdetermined system. However, advanced mathematical methods and algorithms have been successfully developed to reconstruct reasonably good images that have been proven to be of great value in diagnostic radiology.

8.1. RADON TRANSFORM AND IMAGE RECONSTRUCTION

As described in Chapter 2, the Radon transform defines a projection of an object as a collection of ray integrals. Figure 2.15 shows a line integral that is computed along the parallel arrow lines that are sampled along the p axis and are defined by the angle θ. A set of line integrals or projections can be obtained for different θ angles. A projection, $J_\theta(p)$, is periodic in θ with a period of 2π and is also symmetric.

The Radon transform of an object $f(x, y)$ is expressed as the projection $J_\theta(p)$ and is defined as

$$R\{f(x, y)\} = J_\theta(p) = \int_{-\infty}^{\infty} f(p\cos\theta - q\sin\theta, \, p\sin\theta + q\cos\theta)\, dq \qquad (8.1)$$

where p and q form a rotated coordinate system with an angle θ with respect to the x-y coordinate system such that

$$p = x\cos\theta + y\sin\theta$$
$$q = -x\sin\theta + y\cos\theta$$

and

$$x = p\cos\theta - q\sin\theta$$
$$y = p\sin\theta + q\cos\theta. \qquad (8.2)$$

8.1.1 The Central Slice Theorem

The central slice theorem, also called the projection theorem, provides a relationship between the Fourier transform of the object function and the Fourier transform of its Radon transform or projection. Let us continue to assume the object function $f(x, y)$ in two dimensions with one-dimensional (1-D) projections $J_\theta(p)$ defined as the Radon transform of the object function shown in Equation 8.1.

The Fourier transform of the Radon transform of the object function $f(x, y)$ can be written as (5–7)

$$F\{R\{f(x, y)\}\} = F\{J_\theta(p)\} = \int_{-\infty}^{\infty}\int_{-\infty}^{\infty} f(p\cos\theta - q\sin\theta, \, p\sin\theta + q\cos\theta)e^{-j2\pi\omega p}\, dq\, dp \qquad (8.3)$$

where ω represents the frequency component in the Fourier domain.

The Fourier transform, $S_\theta(\omega)$ of the projection $J_\theta(p)$ can also be expressed as

$$S_\theta(\omega) = \int\limits_{-\infty}^{\infty} J_\theta(p)e^{-j2\pi\omega p}dp. \tag{8.4}$$

Substituting Equations 8.2 and 8.3 in Equation 8.4, the Fourier transform of the Radon transform of the object function can be written as

$$S_\theta(\omega) = \int\limits_{-\infty}^{\infty}\int\limits_{-\infty}^{\infty} f(x, y)e^{-j2\pi\omega(x\cos\theta+y\sin\theta)}dx\,dy = F(\omega, \theta). \tag{8.5}$$

Equation 8.5 can be considered as the 2-D Fourier transform of the object function $f(x, y)$ and can be represented as $F(u, v)$ with

$$u = \omega\cos\theta$$
$$v = \omega\sin\theta \tag{8.6}$$

where u and v represent frequency components along the x- and y-directions in a rectangular coordinate system.

It should be noted that $S_\theta(\omega)$ represents the Fourier transform of the projection $J_\theta(p)$ that is taken at an angle θ in the space domain with a rotated coordinate system (p, q). The frequency spectrum $S_\theta(\omega)$ is placed along a line or slice at an angle θ in the frequency domain of $F(u, v)$.

As shown in Figure 8.1, if several projections are obtained using different values of the angle θ, their Fourier transform can be computed and placed along the respective radial lines in the frequency domain of the Fourier transform, $F(u, v)$, of the object function $f(x, y)$. Additional projections acquired in the space domain
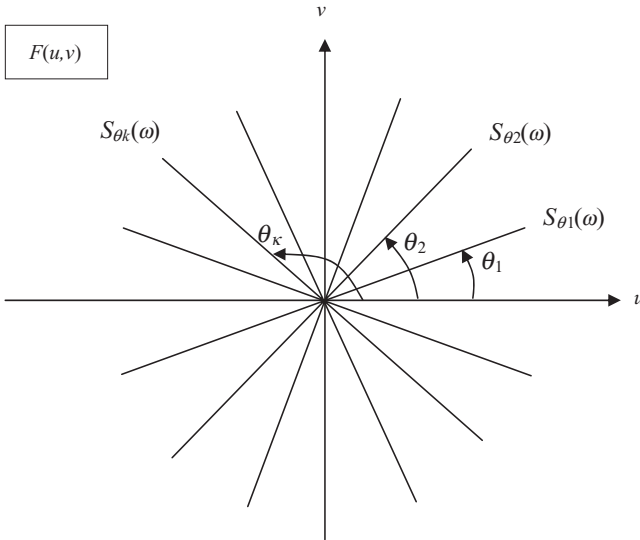

Figure 8.1   The frequency domain of the Fourier transform $F(u, v)$ with the Fourier transforms, $S_\theta(\omega)$ of individual projections $J_\theta(p)$.

provide more spectral information in the frequency domain leading to the entire frequency domain being filled up. Now the object function can be reconstructed using 2-D inverse Fourier transform of the spectrum $F(u, v)$.

8.1.2 Inverse Radon Transform

The forward Radon transform is used to obtain projections of an object function at different viewing angles. Using the central slice theorem, an object function can be reconstructed by taking the inverse Fourier transform of the spectral information in the frequency domain that is assembled with the Fourier transform of the individual projections. Thus, the reconstructed object function, $\hat{f}(x, y)$, can be obtained by taking the 2-D inverse Fourier transform of $f(u, v)$ as

$$\hat{f}(x, y) = F^{-1}\{F(u, v)\} = \int_{-\infty}^{\infty}\int_{-\infty}^{\infty} F(u, v)e^{j2\pi(xu+vy)}du\,dv \qquad (8.7)$$

Representing $\hat{f}(x, y)$ in the polar coordinate system as $\hat{f}(r, \theta)$, Equation 8.7 can be rewritten with the change of variables as

$$\hat{f}(r, \theta) = \int_{0}^{\pi}\int_{-\infty}^{\infty} F(\omega, \theta)e^{j2\pi w(x\cos\theta+y\sin\theta)}\,|\omega|\,d\omega\,d\theta. \qquad (8.8)$$

In Equation 8.8, the frequency variable ω appears because of the Jacobian due to change of variables. Replacing $F(\omega, \theta)$ with $S_\theta(\omega)$, the reconstructed image $\hat{f}(x, y)$, can be expressed as the back-projected integral (sum) of the modified projections $J_\theta^*(p')$ as

$$\hat{f}(r, \theta) = \int_{0}^{\pi}\int_{-\infty}^{\infty} |\omega|\,S_\theta(\omega)e^{j2\pi\omega\,(x\cos\theta+y\sin\theta)}\,d\omega\,d\theta$$

$$= \int_{0}^{\pi} J_\theta^*(p')d\theta$$

where

$$J_\theta^*(p') = \int_{-\infty}^{\infty} |\omega|\,S_\theta(\omega)e^{j2\pi\omega\,(x\cos\theta+y\sin\theta)}\,d\omega. \qquad (8.9)$$

8.1.3 Backprojection Method

Although the object function can be reconstructed using the inverse Fourier transform of the spectral information of the frequency domain $F(u, v)$ obtained using the central slice theorem, an easier implementation of Equation 8.9 can be obtained by its realization through the modified projections, $J_\theta^*(p')$. This realization leads to the convolution–backprojection, also known as filtered backprojection method for image reconstruction from projections.

The modified projection $J_\theta^*(p')$ can be expressed in terms of a convolution of

$$J_\theta^*(p') = \int\limits_{-\infty}^{\infty} |\omega| \, S_\theta(\omega) e^{j2\pi\omega \, (x\cos\theta + y\sin\theta)} \, d\omega$$

$$= \int\limits_{-\infty}^{\infty} |\omega| \, S_\theta(\omega) e^{j2\pi\omega \, p} \, d\omega$$

$$= F^{-1}\{|\omega| \, S_\theta(\omega)\}$$

$$= F^{-1}\{|\omega|\} \otimes J_\theta(p) \tag{8.10}$$

where $\otimes$ represents the convolution operator.

Equation 8.10 presents some interesting challenges for implementation. The integration over the spatial frequency variable ω should be carried out from $-\infty$ to ∞. But in practice the projections are considered to be bandlimited. This means that any spectral energy beyond a spatial frequency, say Ω, must be ignored. With Equations 8.9 and 8.10, it can be shown that the reconstruction function or image, $\hat{f}(x, y)$ can be computed as

$$\hat{f}(x, y) = \frac{1}{\pi} \int\limits_0^{\pi} d\theta \int\limits_{-\infty}^{\infty} dp' \, J_\theta(p')h(p - p') \tag{8.11}$$

where $h(p)$ is a filter function that is convolved with the projection function.

Ramachandran and Lakshiminarayanan (**7**) computed the filter function $h(p)$ strictly from Equation 8.10 in the Fourier domain as

$$H_{R-L} = \begin{cases} |\omega| & \text{if } |\omega| \leq \Omega \\ 0 & \text{otherwise} \end{cases} \tag{8.12}$$

where H_{R-L} is the Fourier transform of the filter kernel function $h_{R-L}(p)$ in the spatial domain and is bandlimited.

In general, $H(\omega)$, a bandlimited filter function in the frequency domain (Fig. 8.2) can be expressed as
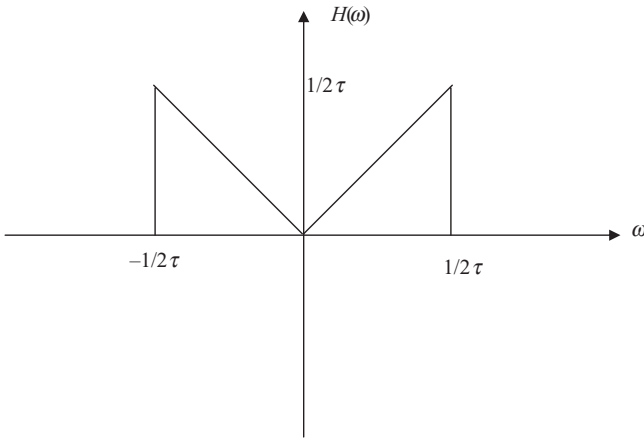

Figure 8.2   A bandlimited filter function $H(\omega)$.

$$H(\omega) = |\omega| B(\omega)$$

where $B(\omega)$ denotes the bandlimiting function

$$B(\omega) = \begin{cases} 1 & \text{if } |\omega| \le \Omega \\ 0 & \text{otherwise} \end{cases}. \tag{8.13}$$

For the convolution operation with the projection function in the spatial domain (Eqs. 8.9 and 8.10), the filter kernel function, $H(\omega)$ can be obtained from $h(p)$ by taking the inverse Fourier transform as

$$h(p) = \int_{-\infty}^{\infty} H(\omega) e^{j2\pi\omega p} \, d\omega. \tag{8.14}$$

If the projections are sampled with a time interval of τ, the projections can be represented as $J_\theta(k\tau)$ where k is an integer. Using the sampling theorem and the bandlimited constraint, all spatial frequency components beyond Ω are ignored such that

$$\Omega = \frac{1}{2\tau}. \tag{8.15}$$

For the bandlimited projections with a sampling interval of t, Equation 8.14 can be expressed with some simplification as

$$h(p) = \frac{1}{2\tau^2} \frac{\sin(\pi p / \tau)}{\pi p / \tau} - \frac{1}{4\tau^2} \left(\frac{\sin(\pi p / 2\tau)}{\pi p / 2\tau} \right)^2. \tag{8.16}$$

Thus, the modified projection $J_\theta^*(p')$ and the reconstruction image can be computed as

$$J_\theta^*(p') = \int_{-\infty}^{\infty} J_\theta(p') h(p - p') \, dp'$$

$$\hat{f}(x, y) = \frac{\pi}{L} \sum_{i=1}^{L} J_{\theta_i}(p') \tag{8.17}$$

where L is the total number of projections acquired during the imaging process at viewing angles θ_i; for $i = 1, \ldots, L$.

The quality of the reconstructed image depends heavily on the number of projections and the spatial sampling interval of the acquired projection. For better quality images to be reconstructed, it is essential to acquire a large number of projections covering the entire range of viewing angles around the object. Higher resolution images with fine details can only be reconstructed if the projections are acquired with a high spatial sampling rate satisfying the basic principle of the sampling theorem. If the raw projection data is acquired at a sampling rate lower than the Nyquist sampling rate, aliasing artifacts would occur in the reconstructed image because of the overlapping spectra in the frequency domain. The fine details in the reconstructed images represent high-frequency components. The maximum frequency component that can be reconstructed in the image is thus limited by the
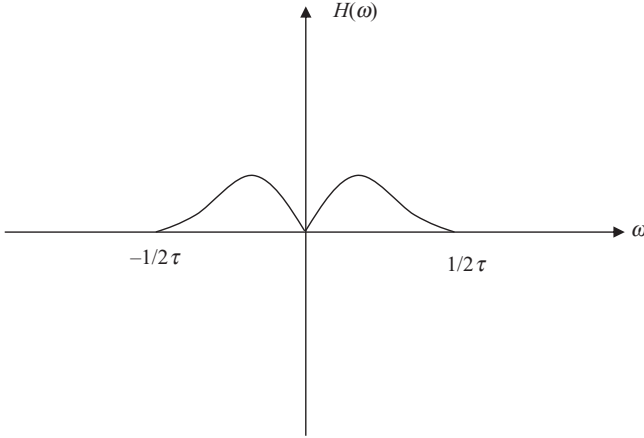
Figure 8.3   A Hamming window based filter kernel function in the frequency domain.

detector size and the scanning procedure used in the acquisition of raw projection data. To reconstruct images of higher resolution and quality, the detector size should be small. On the other hand, the projection data may suffer from poor signal-to-noise ratio (SNR) if there is not sufficient number of photons collected by the detector due to its smaller size.

There are several variations in the design of the filter function $H(\omega)$ investigated in the literature. The acquired projection data is discrete in the spatial domain. To implement the convolution–backprojection method in the spatial domain, the filter function has to be realized as discrete in the spatial domain. The major problem of the Ramachandaran–Lakshiminarayanan filter is that it has sharp cutoffs in the frequency domain at $\omega = 1/2\tau$ and $\omega = -1/2\tau$ as shown in Figure 8.2. The sharp cutoff-based function provides sinc functions for the filter in the spatial domain as shown in Equation 8.16, causing modulated ringing artifacts in the reconstructed image. To avoid such artifacts, the filter function must have smooth cutoffs such as those obtained from Hamming window function. A bandlimited generalized Hamming window can be represented as

$$H_{Hamming}(\omega) = |\omega|\big[\alpha + (1-\alpha)\cos(2\pi\omega\tau)\big]B(\omega) \quad \text{for } 0 \leq \alpha \leq 1 \qquad (8.18)$$

where the parameter α can be adjusted to provide appropriate characteristic shape of the function.

The Hamming window-based filter kernel function provides smoother cutoffs as shown in Figure 8.3. The spatial domain functions for the Ramachandaran–Lakshiminarayanan and Hamming window-based filter kernels (5–7) are shown for comparison in Figure 8.4. It is apparent from Figure 8.4 that the Hamming window-based convolution function provides smoother function in the spatial domain that reduces the ringing artifacts and improves SNR in the reconstructed image. Other smoothing functions can be used to reduce ringing artifacts and improve the quality of the reconstructed image.
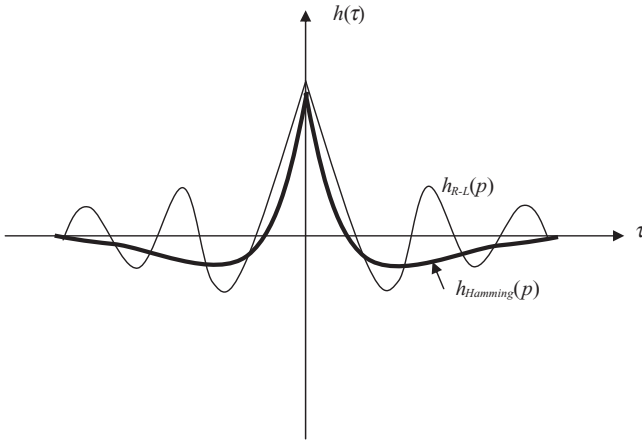
Figure 8.4   A comparison of the $h_{Ham\ min\ g}(p)$ and $h_{R-L}(p)$ convolution functions in the spatial domain.

8.2.   ITERATIVE ALGEBRAIC RECONSTRUCTION METHODS

Although the filtered backprojection method is commonly used for medical image reconstruction, iterative methods are used for image reconstruction as an alternative. The iterative reconstruction methods are based on optimization strategies incorporating specific constraints about the object domain and the reconstruction process. Algebraic reconstruction techniques (ART) are popular algorithms used in iterative image reconstruction. In the algebraic reconstruction methods, the raw projection data from the scanner is distributed over a prespecified image reconstruction grid such that the error between the computed projections from the reconstructed image and the actual acquired projections is minimized. Such methods provide a mechanism to incorporate additional specific optimization criteria such as smoothing and entropy maximization in the reconstruction process to improve the image quality and SNR. The algebraic reconstruction methods are based on the series expansion representation of a function and were used by Gordon and Herman for medical image reconstruction (5, 8).

Let us assume a 2-D image reconstruction grid of N pixels as shown in Figure 8.5. Let us define p_i representing the projection data as a set of ray sums that are collected by M scanning rays passing through the image at specific angles as shown in Figure 8.5. Let f_j be the value of jth pixel of the image that is weighted by $w_{i,j}$ to meet the projection measurements. Thus, the ray sum, p_i, in the projection data can be expressed as

$$p_i = \sum_{j=1}^{N} w_{i,j} f_j \quad \text{for } i = 1, \dots, M. \tag{8.19}$$

Equation 8.19 provides M equations of N unknown variables to be determined. The weight $w_{i,j}$ represents the contribution of the pixel value in determining the ray sum
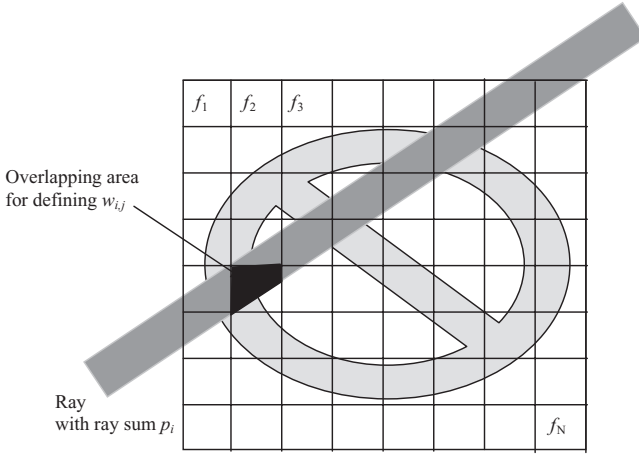
Figure 8.5   Reconstruction grid with a ray defining the ray sum for ART.

and can be determined by geometrical consideration as the ratio of the area overlapping with the scanning ray to the total area of the pixel. The problem of determining f_j for image reconstruction can be solved iteratively using the ART algorithm. Alternately, it can be solved through matrix inversion since the measured projection data p_i is known. The set of equations can also be solved using dynamic programming methods (5).

In algebraic reconstruction methods, each pixel is assigned a predetermined value such as the average of the raw projection data per pixel to start the iterative process. Any time during the reconstruction process, a computed ray sum from the image under reconstruction is obtained by passing a ray as shown in Figure 8.5. In each iteration, an error between the measured projection ray sum and the computed ray sum is evaluated and distributed on the corresponding pixels in a weighted manner. The correction to the pixel values can be obtained in an additive or multiplicative manner; that is, the correction value is either added to the current pixel value or multiplied with it to obtain the next value. The iterative process continues until the error between the measured and computed ray sums is minimized or meets a prespecified criterion. The f_j values from the last iteration provide the final reconstructed image.

Let q_j^k be the computed ray sum in the kth iteration that is projected over the reconstruction grid in the next iteration. The iterative procedure can then be expressed as

$$q_i^k = \sum_{l=1}^{N} f_l^{k-1} w_{i,l} \quad \text{for all } i = 1, \dots, M$$

$$f_j^{k+1} = f_j^k + \left[\frac{p_i - q_i^k}{\sum_{l=1}^{N} w_{i,l}^2} \right] w_{i,j}. \tag{8.20}$$

Gordon (8) used an easier way to avoid large computation of the weight matrix by replacing the weight by 1 or 0. If the center of the pixel passes through the ray, the corresponding weight is assigned as 1, otherwise 0. This simplification provides an efficient implementation of the algorithm and is known as additive ART. Other versions of ART including multiplicative ART have been developed to improve the reconstruction efficacy and quality (5, 8).

The iterative ART methods offer an attractive alternative to the filtered back-projection method because of their abilities to deal with the noise and random fluctuations in the projection data caused by detector inefficiency and scattering. These methods are particularly suitable for limited view image reconstruction as more constraints defining the imaging geometry and prior information about the object can easily be incorporated into the reconstruction process.

8.3.   ESTIMATION METHODS

Although the filtered backprojection methods are most commonly used in medical imaging, in practice, a significant number of approaches using statistical estimation methods have been investigated for image reconstruction for transmission as well as emission computed tomography (ECT). These methods assume a certain distribution of the measured photons and then find the parameters for attenuation function (in the case of transmission scans such as X-ray CT) or emitter density (in the case of emission scans such as PET).

The photon detection statistics of a detector is usually characterized by Poisson distribution. Let us define a measurement vector $\vec{J} = [J_1, J_2, \ldots, J_N]$ with J_i to be the random variable representing the number of photons collected by the detector for the ith ray such that (9)

$$E[J_i] = m_i e^{-\int_L \mu(x,y,z)dl} \quad \text{for } i = 1, 2, \ldots, N \qquad (8.21)$$

where L defines the ray along which the photons with monochromatic energy have been attenuated with the attenuation coefficients denoted by μs milliseconds, and m_i is the mean number of photons collected by the detector for the ith ray position. Also, in the above formulation, the noise, scattering, and random coincidence effects are ignored.

The attenuation parameter vector $\vec{\mu}$ can be expressed in terms of a series expansion as a weighted sum of individual attenuation coefficients of corresponding pixels (for 2-D reconstruction) or voxels (for 3-D reconstruction). If the parameter vector $\vec{\mu}$ has N_p number of individual elements (pixels or voxels), it can be represented as

$$\vec{\mu} = \sum_{j=1}^{N_p} \mu_j w_j \qquad (8.22)$$

where w_j is the basis function that is the weight associated with the individual μ_j belonging to the corresponding pixel or voxel.

One simple solution to obtain w_j is to assign it a value of 1 if the ray contributing to the corresponding photon measurement vector passes through the pixel (or

voxel) and 0 otherwise. It can be shown that a line integral or ray sum for ith ray is given by

$$\int_{L_i} \mu(x, y, z)\, dl = \sum_{k=1}^{N_p} a_{ik}\mu_k \tag{8.23}$$

where $a_{ik} = \int_{L_i} w_k(\bar{x})$ with $\bar{x}$ representing the position vector for (x, y, z) coordinate system.

The weight matrix $A = \{a_{ik}\}$ is defined to rewrite the measurement vector as

$$J_i(\bar{\mu}) = m_i e^{-[A\bar{\mu}]_i} \tag{8.24}$$

where $[A\bar{\mu}]_i = \sum_{k=1}^{N_p} a_{ik}\mu_k$.

The reconstruction problem is to estimate $\bar{\mu}$ from a measured set of detector counts realizing the random variable $\bar{J}$. The maximum likelihood (ML) estimate can be expressed as (9–11)

$$\hat{\bar{\mu}} = \arg\max_{\bar{\mu} \geq \bar{0}} L(\bar{\mu})$$

$$L(\bar{\mu}) = \log P[\bar{J} = \bar{j}; \bar{\mu}) \tag{8.25}$$

where $L(\bar{\mu})$ is the likelihood function defined as the logarithmic of the probability function $P[\bar{J} = \bar{j}; \bar{\mu})$. The ML reconstruction methods are developed to obtain an estimate of the parameter vector $\bar{\mu}$ that maximizes the probability of observing the measured data (photon counts).

Using the Poisson distribution model for the photon counts, the measurement joint probability function $P[\bar{J} = \bar{j}; \bar{\mu})$ can be expressed as

$$P[\bar{J} = \bar{j}; \bar{\mu}) = \prod_{i=1}^{N} P[J_i = j_i; \bar{\mu}) = \prod_{i=1}^{N} \frac{e^{-j_i(\mu)}[j_i(\mu)]^{j_i}}{j_i!}. \tag{8.26}$$

If the measurements are obtained independently through defining ray sums, the log likelihood function can be expressed combining Equations 8.21, 8.25, and 8.26 as

$$L(\bar{\mu}) = \sum_{i=1}^{N} h_i([A\bar{\mu}]_i) \tag{8.27}$$

where $h_i(l) = j_i \log(m_i e^{-1}) - m_i e^{-1}$.

Let us consider an additive non-negative function r_i representing the background photon count for the ith detector due to the scattering and random coincidences; the likelihood function can then be expressed as (9)

$$L(\bar{\mu}) = \sum_{i=1}^{N} h_i([A\bar{\mu}]_i) \tag{8.28}$$

where $h_i(l) = j_i \log(m_i e^{-1} + r_i) - (m_i e^{-1} + r_i)$.

Several algorithms have been investigated in the literature to obtain an estimate of the parameter vector that maximizes the log likelihood function given in Equation 8.27. However, it is unlikely that there is a unique solution to this problem. There may be several solutions of the parameter vector that can maximize the likelihood function. All solutions may not be appropriate or even feasible for image

reconstruction. To improve quality of reconstructed images, a number of methods imposing additional constraints such as smoothness are applied by incorporating the penalty functions in the optimization process. Several iterative optimization processes incorporating roughness penalty function for the neighborhood values of the estimated parameter vector have been investigated in the literature (9–11).

Let us represent a general roughness penalty function $R(\mu)$ (9, 10) such that

$$R(\vec{\mu}) = \sum_{k=1}^{K} \psi([\mathbf{C}\vec{\mu}]_k) \tag{8.29}$$

where $[\mathbf{C}\vec{\mu}]_k = \sum_{l=1}^{N_p} c_{kl}\mu_l$

where ψ_k are potential functions working as a norm on the smoothness constraints $C\mu \approx 0$ and K is the number of such constraints. The matrix $\mathbf{C}$ is a $K \times N_p$ penalty matrix. It should be noted that ψ_k are convex, symmetric, non-negative, and differentiable functions (9). A potential choice for a quadratic penalty function could be by defining $\psi_k(t) = w_k t^2/2$ with non-negative weights, that is, $w_{k \geq 0}$. Thus, the roughness penalty function $R(\vec{\mu})$ is given by

$$R(\vec{\mu}) = \sum_{k=1}^{K} w_k \frac{1}{2}([\mathbf{C}\vec{\mu}]_k)^2. \tag{8.30}$$

The objective function for optimization using the penalized ML approach can now be revised as

$$\hat{\vec{\mu}} = \arg\max \Phi(\vec{\mu}) \tag{8.31}$$

where $\Phi(\vec{\mu}) = L(\vec{\mu}) - \beta R(\vec{\mu})$.

The parameter β controls the level of smoothness in the final reconstructed image.

Several methods for obtaining the above ML estimate have been investigated in the literature. These optimization methods include expectation maximization (EM), complex conjugate gradient, gradient descent optimization, grouped coordinated ascent, fast gradient-based Bayesian reconstruction, and ordered-subsets algorithms (12–21). Such iterative algorithms have been applied to obtain a solution for the parameter vector for reconstructing an image from both transmission and emission scans.

In general, the penalized function $\Phi(\vec{\mu})$ is quite complex and difficult to optimize. De Pierro (22) used an optimization transfer method defining a surrogate function $\phi(\vec{\mu}; \vec{\mu}^{(n)})$ that is easier to optimize with an estimate of attenuation vector after the nth iteration represented by $\vec{\mu}^{(n)}$. There are many choices for surrogate functions. For example, a parabola surrogate function with an optimal curvature to ensure fast optimization process can be designed (9, 10). A quadratic surrogate function may be defined as

$$q(l; l_i^{(n)}) \equiv h(l_i^{(n)}) + \dot{h}(l_i^{(n)})(l - l_i^{(n)}) - \frac{c}{2}(l - l_i^{(n)})^2$$

$$\text{for} \quad c \geq 0 \quad and \quad l_i^{(n)} = [A\vec{\mu}]_i \tag{8.32}$$

The variable $l_i^{(n)}$ is the ith line integral through the estimated attenuation map at the nth iteration.

The estimation problem can then be rewritten involving the surrogate function in each iteration as

$$\phi(\vec{\mu}; \vec{\mu}^{(n)}) \equiv Q(\vec{\mu}; \vec{\mu}^{(n)}) - \beta R(\vec{\mu}) \tag{8.33}$$

where $Q(\vec{\mu}; \vec{\mu}^{(n)})$ is the conditional expectation of log-likelihood function in the nth iteration.

The function $Q(\vec{\mu}; \vec{\mu}^{(n)})$ can be provided (9) as

$$Q(\vec{\mu}; \vec{\mu}^{(n)}) = \sum_{k=1}^{N_p} Q_k(\mu_k; \vec{\mu}^{(n)})$$

where

$$Q_k(\mu_k; \vec{\mu}^{(n)}) = \sum_{i=1}^{N} \bar{N}_{ik}^{(n)} \log(e^{-a_{ik}\mu_k}) + (\bar{M}_{ik}^{(n)} - \bar{N}_{ik}^{(n)})\log(1 - e^{-a_{ik}\mu_k})$$

$$\bar{N}_{ik}^{(n)} \equiv E[J_{il}/J_i = j_i; \vec{\mu}^{(n)}]|_{l:k_{i,l}=j}$$

$$\bar{M}_{ik}^{(n)} \equiv E[J_{il-1}/J_i = j_i; \vec{\mu}^{(n)}]|_{l:k_{i,l}=j} \tag{8.34}$$

Now, the EM algorithm can be expressed as the implementation of the following steps in each iteration until convergence:

1. **E-Step:**

$$\text{Find } Q(\vec{\mu}; \vec{\mu}^{(n)}) \text{ and } \phi(\vec{\mu}; \vec{\mu}^{(n)})$$

2. **M-Step:**

$$\vec{\mu}^{(n+1)} = \arg\max_{\vec{\mu}} \phi(\vec{\mu}; \vec{\mu}^{(n)}) \tag{8.35}$$

By combining these steps with the surrogate function, it can be shown (9) that the iterative ML–EM estimate for the transmission scans can be given as

$$\mu_k^{(n+1)} = \frac{\displaystyle\sum_{i=1}^{N} (\bar{M}_{ik}^{(n)} - \bar{N}_{ik}^{(n)})}{\dfrac{1}{2} \displaystyle\sum_{i=1}^{N} a_{ik}(\bar{M}_{ik}^{(n)} + \bar{N}_{ik}^{(n)})} \tag{8.36}$$

8.4. FOURIER RECONSTRUCTION METHODS

As described above, the central slice theorem provides a relationship between the projection acquired in the rotated coordinate system and the Fourier domain of the object. For 2-D image reconstruction, the 1-D Fourier transform of the projection acquired at an angle θ belongs to the corresponding radial line at the same angle in the 2-D Fourier transform (represented in the polar coordinate system) of the object. If a sufficient number of projections are obtained, their respective Fourier transforms can be placed in the frequency domain as shown in Figure 8.1. This 2-D

representation of the frequency information usually requires a great deal of interpolation with the change from polar to Cartesian coordinate systems. This is a necessary and computationally expensive step to fill the frequency space evenly to avoid artifacts in the reconstructed images. To reconstruct the image in the spatial domain, a 2-D inverse Fourier transform is applied to this interpolated information in the frequency domain.

The choice of interpolation function is critical in the direct Fourier reconstruction methods. Recently, sinc function-based gridding algorithms for fast Fourier reconstruction have been investigated (23, 24). The Fourier reconstruction method using the central slice theorem resamples the frequency domain information from a polar to a Cartesian grid. Walden used Shannon sampling theorem for developing sinc function-based interpolation method for the bandlimited functions in the radial direction. The interpolation in the angular direction was done with standard methods such as polynomial interpolation (25).

8.5. IMAGE RECONSTRUCTION IN MEDICAL IMAGING MODALITIES

To reconstruct images in a specific medical imaging modality, it is necessary to consider the data collection process. Filtered backprojection methods are ideal for transmission scans such as X-ray CT but do not provide a theoretically sound basis for image reconstruction for ECT. The probabilistic nature of the emission process is well suited for statistical estimation method-based image reconstruction techniques. However, the estimation-based image reconstruction methods are relatively complex and computationally expensive. Noise and detector variability cause additional problems in image reconstruction with respect to unique convergence of iterative estimation-based image reconstruction methods. Because of these difficulties, filtered backprojection methods have been modified for emission imaging and are commonly used for practical image reconstruction in single photon emission computed tomography (SPECT) and positron emission tomography (PET). However, new ML and EM approaches are attractive, provide good results, and are expected to take a more prominent role in practical image reconstruction.

Specific image reconstruction methods for medical imaging modalities are described in the following subsections.

8.5.1 Image Reconstruction in X-Ray CT

The filtered backprojection method is most commonly used in X-ray CT for image reconstruction. The method described above essentially deals with the projections obtained in parallel-beam geometry. However, recent scanners use a divergent 2-D or 3-D beam for imaging. Thus, the data obtained from the divergent beams have to be resorted before the filtered backprojection method developed for parallel projections is applied. It should be noted that each ray in the divergent beam can be reorganized in a specific projection in the parallel-beam geometry. Figure 8.6 shows a 2-D divergent beam with the angular step γ and the radial distance D between the
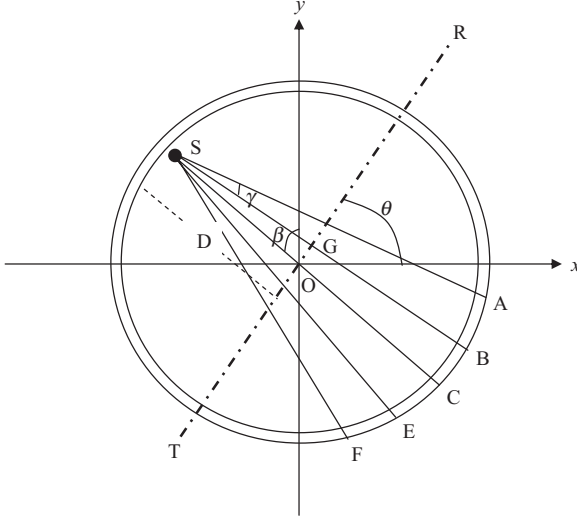
Figure 8.6 A 2-D divergent beam geometry.

source and the origin. This geometry is well suited for fourth-generation CT scanners in which the detectors are placed along circular ring(s).

Let $K_\beta(\gamma)$ represent a fan projection from the divergent beam where β is the angle that the source makes with its central reference axis and γ indicates the location of the ray as shown in Figure 8.6. The objective of the resorting algorithm is to convert fan projections $K_\beta(\gamma)$ into the parallel-beam projection representation $J_\theta(p)$ as defined earlier in this chapter. In Figure 8.6, a plane R-T is shown at an angle θ over which a parallel projection $J_\theta(p)$ is computed using the rotated coordinate system. Considering the ray SB intersecting the parallel projection plane R-T at G, it can be noted that

$$\theta = \beta + \gamma \quad \text{and} \quad OG = p = D\sin\gamma. \tag{8.37}$$

The fan projections $K_\beta(\gamma)$ can be sorted into $K'_\beta(\gamma)$ corresponding to the parallel-beam geometry suitable for implementation of the filtered backprojection method. The sorting relationship for all source positions denoted by β_i can be expressed as

$$K'_{\beta_i}(\gamma) = K_{\beta_i}(\gamma)D\cos\gamma. \tag{8.38}$$

For image reconstruction, $K'_{\beta_i}(\gamma)$ is convolved with the filter function $h(\gamma)$ to provide filtered projections $Q_{\beta_i}(\gamma)$ that are backprojected as

$$Q_{\beta_i}(\gamma) = K'_{\beta_i}(\gamma) \otimes h(\gamma)$$

$$f(x, y) = \Delta\beta \sum_{i=1}^{N} \frac{1}{L^2(x, y; \beta_i)} Q_{\beta_i}(\gamma') \tag{8.39}$$

where N is the total number of source positions, $L\,\gamma'$ is the angle of the divergent beam ray passing through the point (x, y), and L is the distance between the source and the point (x, y) for the source position β_i.

Recently, cone-beam geometry has been investigated for CT imaging and image reconstruction. A cone beam is a 3-D divergent beam to scan an entire or partial volume of a 3-D object. Cone-beam reconstruction method is basically derived from fan-beam geometry with the additional third dimension. However, the mathematical methods for image reconstruction from cone-beam data become complicated, requiring heuristics to deal with the uncertainties of the data mapping and interpolation issues (26). Also, a direct backprojection algorithm of 3-D Radon transform can be found in Reference (27). In this method, the 3-D Radon transform-based backprojection operation is recursively decomposed using a hierarchical approach.

8.5.2 Image Reconstruction in Nuclear Emission Computed Tomography: SPECT and PET

Although the basic principles of image reconstruction in ECT are the same as X-ray CT, there is an important difference in these two modalities regarding the parameter to be reconstructed. The objective of image reconstruction in X-ray CT is to estimate the attenuation coefficient map from the projection data while scattering is usually ignored. In case of image reconstruction in SPECT or PET, the basic objective is to reconstruct the source emission map within the object from the statistical distribution of photons that have gone through attenuation within the object but detected outside the object. In X-ray CT, the source statistics are known with a single unknown parameter of attenuation coefficients. In ECT (SPECT and PET), both source statistics and attenuation coefficient parameters are unknown. Since the distribution of the emission source is to be reconstructed, the attenuation coefficient parameter has to be assumed or estimated. Incorporation of attenuation information in the reconstruction process is called the attenuation correction. Reconstructed images without adequate attenuation corrections are noisy and poor in image quality. There are several methods for attenuation correction used in SPECT image reconstruction (28–32).

In real cases, the attenuation coefficients are nonuniformly distributed within the object. In cases where attenuation coefficients can be assumed to be constant within the object, the attenuation effect can be compensated by taking the arithmetic or geometric mean of the photon counts from a pair of detectors placed in opposite directions (30). Such methods are very efficient in preprocessing the data for attenuation compensation before the filtered backprojection algorithm is applied. However, they provide acceptable results only in low-resolution imaging applications such as full-body imaging. For specific organ imaging, a transmission scan is done to estimate the attenuation coefficient parameter, which is then used in the reconstruction process.

The transmission scans in SPECT for computing the attenuation coefficient parameter usually suffer from low photon statistics and scattering effects. Although filtered backprojection methods are applied with some modification to reconstruct transmission images in SPECT because of computational efficiency, the iterative ML estimation-based algorithms have provided better results (17–19). These algorithms can be used to estimate the attenuation coefficient parameter from the transmission

scan separately or in conjunction with the iterative statistical algorithms for estimation of source distribution for image reconstruction (19).

The current practice in SPECT and PET imaging is to obtain separate transmission scans to compute attenuation maps. However, attenuation maps could be obtained directly from the emission scans by applying the consistency conditions using the projection operator (31, 32).

8.5.2.1   A General Approach to ML–EM Algorithms

The ML-based reconstruction algorithms such as ML–EM find an estimate of the photon emission distribution such that its projections are as close as possible to the measured projection data. A general ML–EM algorithm for ECT is described below (12–14).

Let us assume that the object to be reconstructed has an emission density function $\lambda(x, y, z) = \vec{\lambda} = [\lambda_1, \lambda_2, \ldots, \lambda_B]^t$ with a Poisson process over a matrix of B spatially distributed boxes in the object space or pixels in the reconstruction space. The emitted photons (in case of SPECT) or photon pairs (in case of PET) are detected by the detectors with the measurement vector $\vec{J} = [J_1, J_2, \ldots, J_D]^t$ with D measurements. The problem is then to estimate $\lambda(b)$; $b = 1, \ldots, B$ from the measurement vector.

Each emission in box b is detected by the detector d (SPECT) or the detector tube d (PET) with a probability $p(b, d) = P(\text{detection in } d \text{ for a photon emitted in } b)$. The transition matrix $p(b, d)$ is derived from the geometry of the detector array and the object or reconstruction space.

Let $j(b, d)$ denote the number of emissions in box b detected in the detector or detector tube d. These are independent Poisson variables with the expected value $E[j(b, d)] = \lambda(b, d) = \lambda(b)p(b, d)$.

The likelihood function (13) is defined as

$$L(\lambda) = P(\vec{j} \mid \vec{\lambda}) = \sum_A \prod_{\substack{b=1,\ldots,B \\ d=1,\ldots,D}} e^{-\lambda(b,d)} \frac{\lambda(b, d)^{j(b,d)}}{j(b, d)!} \tag{8.40}$$

where the sum is over all possible detector arrays A of $j(b, d)$.

It can be shown that $L(\lambda)$ is concave (13). An iterative scheme based on the EM algorithm can be used to maximize $L(\lambda)$. The algorithm starts with an initial guess $\lambda^0(b)$ and then, in each iteration, a new estimate $\hat{\lambda}^{new}(b)$ is computed from $\hat{\lambda}^{old}(b)$, the current estimate of $\lambda(b)$ by

$$\hat{\lambda}^{new}(b) = \hat{\lambda}^{old}(b) \sum_{d=1}^{D} \frac{j(d)p(b, d)}{\sum_{b'=1}^{B} \hat{\lambda}^{old}(b')p(b', d)}; \quad b = 1, \ldots, B. \tag{8.41}$$

The general convergence of the above ML–EM algorithm is quite slow and sensitive to the noise in the iteration process. As described above, the ML reconstruction process in emission imaging is an ill-posed problem and can provide a number of solutions fitting the projection data. Some of these solutions are not appropriate and cause large variations when the iteration process continues. Regularization methods such as penalized likelihood estimation, weighted least squares, ordered subsets, and Bayesian estimation algorithms have been applied to obtain a better reconstruction

(19–21). A multigrid EM reconstruction algorithm to improve the efficiency and quality of image reconstruction was investigated with the multiresolution approach using the standard interpolation functions and wavelets (33, 34).

8.5.2.2 A Multigrid EM Algorithm A multigrid expectation maximization (MGEM) algorithm has been applied to the problem of image reconstruction in PET (33). The MGEM algorithm uses the ML–EM method on a set of reconstruction grids with different resolutions. The wavelet-based multiresolution EM algorithm uses wavelet transform for the transition criterion for switching the resolution level. A wavelet spline interpolation method is used to project intermediate reconstructions from a specific grid level to the next finer grid (34).

Let us assume there are a number of grids, G^k, where $k = 1, \ldots, K$ represents the same reconstruction space at different resolutions. G^0 is the coarsest grid while G^K is the finest resolution grid. The reconstruction pyramid consists of square grids of size S^k, $k = 1, \ldots, K$, such that the ratio, $S^{k+1}:S^k = 1:2$. The maximum frequency, f^k, of the image on grid G^k is given by $1/2S^k$, which is twice the maximum frequency that can be represented by G^{k-1}. By using the hierarchical structure of the reconstruction pyramid, the low-frequency components of the finest resolution are recovered quickly at the coarser grids. The problem of slow convergence of the single-grid EM algorithm can then be solved by appropriate utilization of different grid sizes. The low-frequency components are recovered first, using the coarser grids, and then the high-frequency components are recovered by projecting the solutions onto finer grids and reconstructing using the single-grid EM algorithm. Since coarser grid solutions can be found much faster, the MGEM algorithm is computationally much more efficient. Also, some a priori information can be incorporated into the initialization step to reduce the pattern dependency of the EM algorithm. A flow diagram of the MGEM algorithm is shown in Figure 8.7.

The wavelet based multiresolution expected maximization (WMREM) algorithm performs a wavelet based-decomposition of the reconstructed image at each iteration and the energy of the high-high-frequency band of the wavelet decomposition provides the transition criterion to switch to the next grid level. The energy in the high-high-frequency band represents the high-frequency content of the image at that grid level. The grid level is switched when the energy in this band ceases to increase. The switching of the grid levels is continued until a grid level finer than the desired resolution is reached. This is done in order to retrieve the high-frequency components of the desired grid resolution, which are the low frequency components of a grid level finer than the desired grid resolution. The low-low-frequency component of the wavelet decomposition of the reconstructed image is the final image at the desired grid level.

Wavelet-based interpolation methods have been used for several applications (35–39). For the class of smooth functions used in regularization, the ideal basis for transformation would be both spatially and spectrally localized and fast to compute. The desire for spectral localization stems from the fact that the projection of a system onto a spectrally localized basis tends to produce a well-conditioned system. The spatial localization requirement stems from the requirement that the basis vectors must compactly describe the available data. Figure 8.8 shows a wavelet-based interpolation method. Figure 8.9 shows a Shepp and Logan phantom and reconstructed
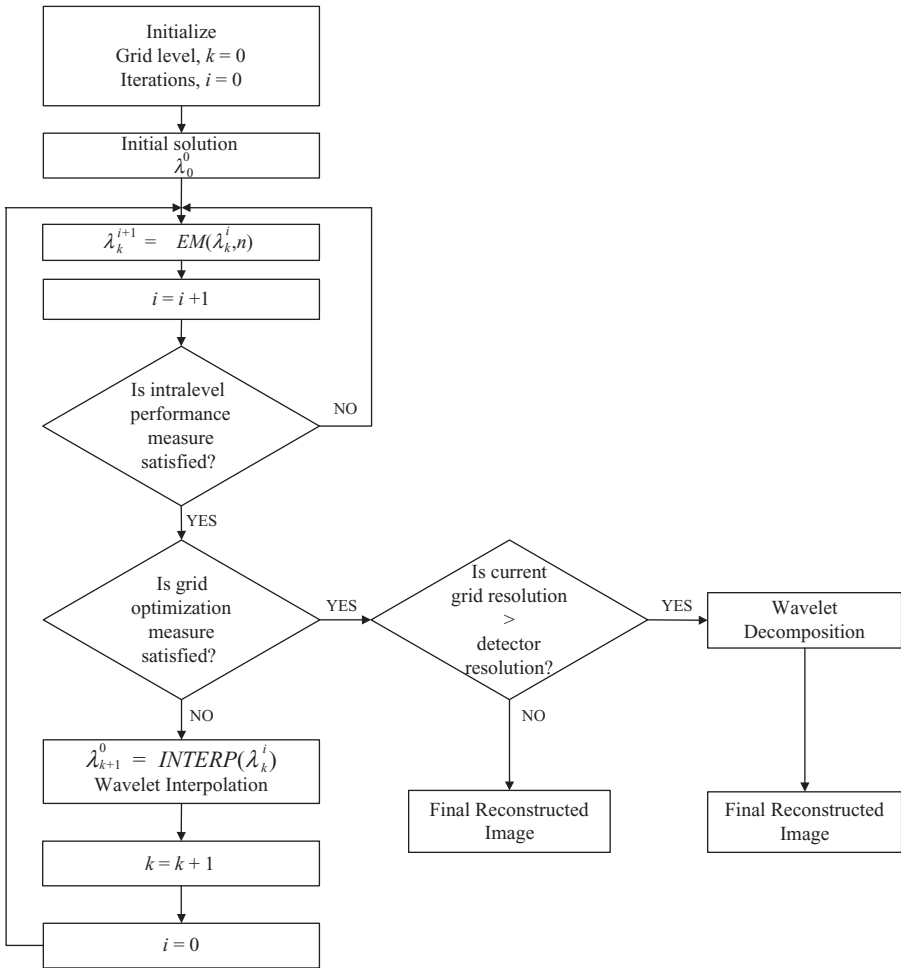
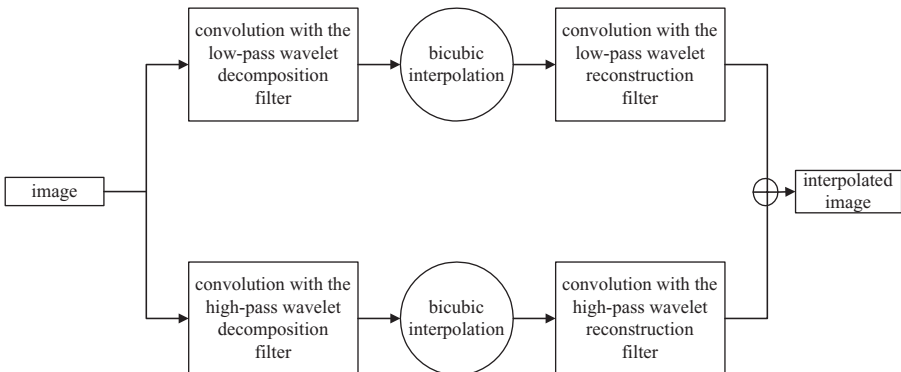Figure 8.7   A flowchart of the MGEM algorithm for PET image reconstruction.

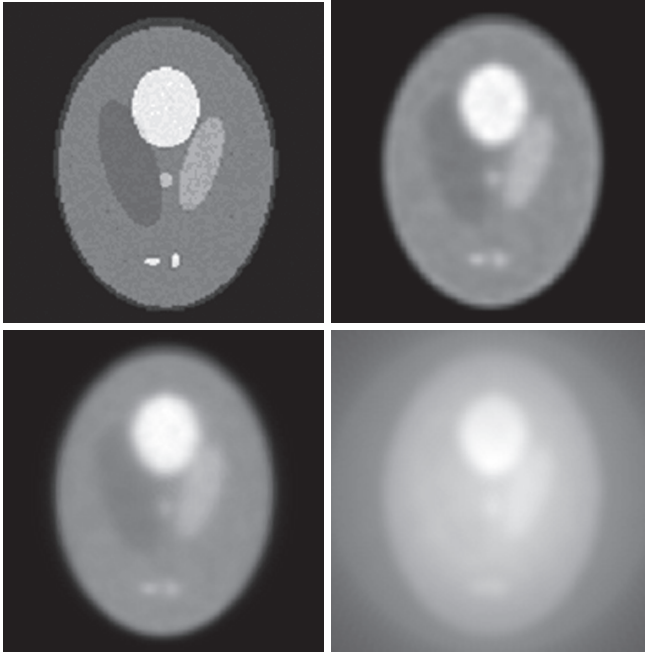Figure 8.8   A wavelet-based interpolation method.

Figure 8.9   Shepp and Logan phantom (top left) and reconstructed phantom images using WMREM algorithm (top right), ML–EM algorithm (bottom left), and filtered backprojection method (bottom right).

images from the ML–EM algorithm (13), WMREM algorithm (35), and the filtered backprojection method. Figure 8.10 shows reconstructed brain images from a PET scan of a patient with a tumor, using a generalized EM algorithm, the backprojection method, and the WMREM algorithm for comparison.

8.5.3   Image Reconstruction in Magnetic Resonance Imaging

The Fourier reconstruction method is commonly applied in magnetic resonance imaging (MRI) for image reconstruction. The electromagnetic free induction decay (FID) signal acquired in MRI image is in the frequency domain. As presented in Equation 5.19 in Chapter 5, the signal $S(\vec{\omega}) = S(\omega_x, \omega_y, \omega_z)$ can be expressed as

$$S(\vec{\omega}) = \vec{M}_0 \iiint f(x, y, z) e^{-i(\omega_x x + \omega_y y + \omega_z z)} dx\, dy\, dz \qquad (8.42)$$

where $f(x, y, z)$ is the image to be reconstructed. For 2-D image reconstruction, the image function is reduced to $f(x, y)$.

Inverse Fourier transform of the signal $S(\vec{\omega})$ provides the reconstructed image. However, this is implemented using discrete fast Fourier transform (FFT) algorithms that may require interpolation of data points depending on the resolution of the reconstructed image and data samples in the k-space. Gridding interpolation algorithms may be used for this purpose (23–25). Specific parameter-based images (such as proton-density, T_1-weighted, and T_2-weighted images) are reconstructed using
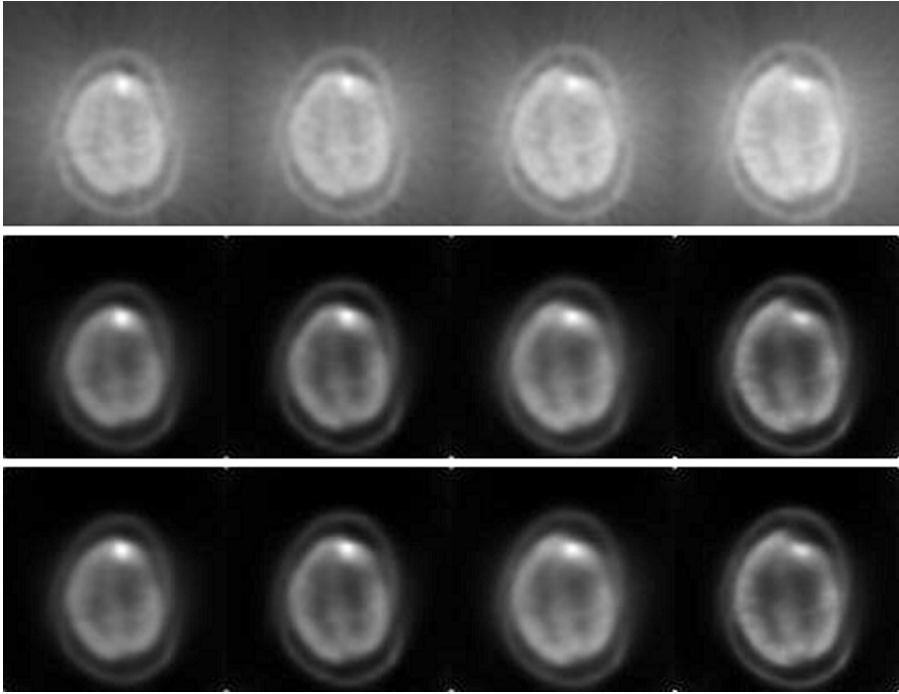
Figure 8.10   Four PET-reconstructed axial brain images of a patient with a tumor. Images in the top row are reconstructed using filtered backprojection method; images in the middle row are reconstructed using WMREM algorithm; and images in the bottom row are reconstructed using a generalized ML–EM algorithm for the same axial cross-sections.

appropriate pulse sequences to acquire the desired signal as explained in Chapter 5, but the image reconstruction method remains the same. Special preprocessing and correlation methods are used in blood flow imaging or functional MRI (fMRI) using the snapshot pulse sequencing, such as spiral echo planar imaging (SEPI), for fast imaging (40, 41). A signal estimation-based analysis in fMRI is discussed in Reference (42).

An important aspect of blood flow imaging or fMRI is that the snapshot pulse sequence (SEPI) has to acquire the entire signal in the k-space in a very short time. The k-space is filled in a spiral geometry by a SEPI sequence as discussed in Chapter 5. Acquisition of all data samples in the k-space in a short time causes other off-resonance effects such as chemical shift and field inhomogeneities to be accumulated, degrading the MR signal. To compensate for these effects, an iterative reconstruction method using ART is presented in Reference (43).

8.5.4   Image Reconstruction in Ultrasound Imaging

Ultrasound imaging is primarily based on the point measurements as described in Chapter 7. The point-by-point measurements lead to a line scan. A collection of line scans can provide a 2-D ultrasound image. Ultrasound arrays can be used to obtain

line measurements more efficiently. To improve the quality of ultrasound image, the most important issue is the reduction of speckle noise. Ultrasound speckle-reduction methods can be characterized into two categories: image averaging and image filtering. In the first approach, several images of a target object are averaged to improve the SNR. It is apparent that such methods suffer from the loss of spatial resolution. Various filters such as weighted median and Wiener filters are used in the second approach to reduce speckle noise (44–46).

Three-dimensional image reconstruction in ultrasound imaging is usually obtained by stacking up 2-D images in the third dimension (47, 48). The difficulty of this approach is the localization of 2-D images in the desired plan to accurately register and interpolate 2-D images for visualization of 3-D structures. In addition, the optimal 2-D image plane may be restricted by the patient's anatomy such that the acquisition of 2-D images along the desired axis may not be feasible. The acquired 2-D images are tagged with some visual landmarks, which are then used for registration using the translation, scaling, and rotation parameters, discussed in Chapter 2. However, the 3-D image reconstruction in ultrasound imaging from 2-D tomographic images suffer from uncertainties in imaging geometry and variability of the structures in the imaging medium. Geometrical distortions and signal variances in 3-D ultrasound image reconstruction from stacking of parallel 2-D images are discussed in Reference (49).

8.6.   EXERCISES

8.1. Assume an object $f(x, y)$ in x–y coordinate system with parallel rays passing through the object at an angle θ. Define a projection $J_\theta(p)$ graphically and express it in mathematical terms using the Radon transform.

8.2. How does a set of projections $J_\theta(p)$ with different viewing angles (with rotated coordinates) relate to the Fourier transform of the object $f(x, y)$?

8.3. Describe a direct Fourier reconstruction method using the central slice theorem.

8.4. Write and describe the mathematical expression of image reconstruction using the backprojection method. Why is there a need for filtering operation in the backprojection reconstruction method?

8.5. What should be the properties of an ideal filter function for the filtered backprojection method? Describe a filter function of your choice and explain the reasons for your selection.

8.6. Implement the filtered backprojection method selected in Exercise 8.5 in the MATLAB environment. Use the Shepp and Logan phantom as an object for image reconstruction. Compute projections every 20 degrees from the Shepp and Logan phantom.

8.7. Repeat Exercise 8.6 with the R-L filter defined in Equation 8.12 to reconstruct Shepp and Logan phantom. Compare and comment on the quality of the reconstructed image with the image obtained in Exercise 8.6.

8.8. Repeat Exercise 8.6 with projections computed every 5 degrees. Compare the reconstructions to those obtained in Exercise 8.6. Comment on the aliasing artifacts, if any.

8.9. What is the significance of interpolation in rebinning algorithm for divergent beam-based projection data to implement parallel-beam based filtered backprojection method?

8.10. What is the basis for iterative algebraic reconstruction methods? What are the advantages and disadvantages of ART compared with the filtered backprojection method?

8.11. Derive an expression for the correction factor for multiplicative ART. Is it a better algorithm than the additive ART? Explain your answer.

8.12. Repeat Exercise 8.6 with the additive ART and compare the reconstructed images with those obtained using the filtered backprojection method. Also, compare the reconstruction error and computation time for ART and filtered backprojection methods.

8.13. Why is attenuation correction important in image reconstruction for SPECT imaging?

8.14. Define an objective function for the penalized ML–EM algorithm for PET. What is the significance of the penalty function? What are the required mathematical properties of the penalty function?

8.15. What is the optimization transfer principle? How does it help in the optimization of the objective function in Exercise 8.11?

8.16. Implement the image reconstruction method for the optimization of the objective function in Exercise 8.11 in the MATLAB environment using a Shepp and Logan phantom for 1 million events of photon emission for 720 detectors and a reconstruction grid of 512×512. Comment on the reconstructed image quality and error in reconstruction by comparing intensity profiles for three oblique cross-sections of the phantom.

8.17. Obtain three multiresolution reconstructions on 64×64, 128×128, and 256×256 separately and compare the reconstruction errors for three reconstruction interpolated to the 512×512 resolution. Use a wavelet-based interpolation method in the MATLAB environment as described in Figure 8.7.

8.7. REFERENCES

1. J. Radon, "Uber die Bestimmung von Funktionen durch ihre Integralwerte langs gewisser Mannigfaltigkeiten," *Ber. Verb. Saechs. AKAD. Wiss., Leipzig, Match Phys.*, Kl 69, pp. 262–277, 1917.
2. G.N. Hounsfield, "A method and apparatus for examination of a body by radiation such as X or gamma radiation," Patent 1283915, The Patent Office, London, England, 1972.
3. G.N. Hounsfield, "Computerized transverse axial scanning tomography: Part-1, description of the system," *Br. J. Radiol.*, Vol. 46, pp. 1016–1022, 1973.
4. A.M. Cormack, "Representation of a function by its line integrals with some radiological applications," *J. Appl. Phys.*, Vol. 34, pp. 2722–2727, 1963.

5. G.T. Herman, *Image Reconstruction from Projections*, Academic Press, New York, 1980.

6. A. Rosenfeld and A.C. Kak, *Digital Picture Processing:* Volume 1, Academic Press, Orlando, FL, 1982.

7. G.N. Ramachandran and A.V. Lakshminaryanan, "Three-dimensional reconstruction from radiographs and electron micrographs," *Proc. Nat. Acad. Sci. USA*, Vol. 68, pp. 2236–2240, 1971.

8. R. Gordon, "A tutorial on ART (algebraic reconstruction techniques)," *IEEE Trans. Nucl. Sci.*, Vol. 21, pp. 78–93, 1974.

9. J.A. Fessler, "Statistical image reconstruction methods for transmission tomography," in M. Sonka and J.M. Fitzpatrick (Eds), *Handbook of Medical Imaging:* Volume 2, *Medical Image Processing and Analysis*, SPIE Press, Bellingham, WA, pp. 1–70, 2000.

10. H. Erdogen and J. Fessler, "Monotonic algorithms for transmission tomography," *IEEE Trans. Med. Imaging*, Vol. 18, pp. 801–814, 1999.

11. D.F. Yu, J.A. Fessler, and E.P. Ficaro, "Maximum likelihood transmission image reconstruction for overlapping transmission beams," *IEEE Trans. Med. Imaging*, Vol. 19, pp. 1094–1105, 2000.

12. A.P. Dempster, N.M. Laird, and D.B. Rubin, "Maximum likelihood from incomplete data via the EM algorithm," *J. R. Stat. Soc. Ser. B*, Vol. 39, pp. 1–38, 1977.

13. L.A. Shepp and Y. Vardi, "Maximum likelihood reconstruction for emission tomography," *IEEE Trans. Med. Imaging*, Vol. 1, pp. 113–121, 1982.

14. K. Lange and R. Carson, "EM reconstruction algorithms for emission and transmission tomography," *J. Comput. Assist. Tomogr.*, Vol. 8, pp. 306–316, 1984.

15. J.M. Olinger, "Maximum likelihood reconstruction of transmission images in emission computed tomography via the EM algorithm," *IEEE Trans. Med. Imaging*, Vol. 13, pp. 89–101, 1994.

16. C.A. Bouman and K. Saur, "A unified approach to statistical tomography using coordinate descent optimization," *IEEE Trans. Image Process.*, Vol. 5, pp. 480–492, 1996.

17. J. Fessler, E. Ficaro, N.H. Climhome, and K. Lange, "Grouped coordinate ascent algorithms for penalized likelihood transmission image reconstruction," *IEEE Trans. Med. Imaging*, Vol. 16, pp. 166–175, 1997.

18. H. Erdogen, G. Gualtiere, and J.A. Fessler, "Ordered subsets algorithms for transmission tomography," *Phys. Med. Biol.*, Vol. 44, pp. 2835–2851, 1999.

19. E.U. Mumcuoglu, R. Leahy, S.R. Cherry, and Z. Zhou, "Fast gradient-based methods for Bayesian reconstruction of transmission and emission PET images," *IEEE Trans. Med. Imaging*, Vol. 13, pp. 687–701, 1994.

20. T. Hebert and R. Leahy, "A generalized EM algorithm for 3-D Bayesian reconstruction from Poisson data using Gibbs priors," *IEEE Trans. Med. Imaging*, Vol. 8, pp. 194–202, 1989.

21. P.J. Green, "Bayesian reconstructions from emission tomography data using a modified EM algorithm," *IEEE Trans. Med. Imaging*, Vol. 9, pp. 84–93, 1990.

22. A.R. De Pierro, "A modified expectation maximization algorithm for penalized likelihood estimation in emission tomography," *IEEE Trans. Med. Imaging*, Vol. 14, pp. 132–137, 1995.

23. J.D. O'Sullivan, "A fast sinc function gridding algorithm for Fourier inversion in computed tomography," *IEEE Trans. Med. Imaging*, Vol. 4, pp. 200–207, 1985.

24. H. Schomberg and J. Timmer, "The gridding method for image reconstruction by Fourier transformation," *IEEE Trans. Med. Imaging*, Vol. 14, pp. 595–607, 1995.

25. J. Walden, "Analysis of the direct Fourier method for computed tomography," *IEEE Trans. Med. Imaging*, Vol. 19, pp. 211–222, 2000.

26. B. Smith and C. Peck, "Implementation, comparison and investigation of heuristic techniques for cone beam tomography," *IEEE Trans. Med. Imaging*, Vol. 15, pp. 519–531, 1996.

27. S. Basu and Y. Bresler, "$O(N^3 \log N)$ Backprojection algorithm for the 3-D Radon transform," *IEEE Trans. Med. Imaging*, Vol. 21, pp. 76–88, 2002.

28. A.V. Bronnikov, "Approximate reconstruction of attenuation map in SPECT imaging," *IEEE Trans. Nucl. Sci.*, Vol. 42, pp. 1483–1488, 1995.

29. B.M.W. Tsui, G.T. Gulberg, E.R. Edgerton, J.G. Ballard, J.R. Perry, W.H. McCartney, and J. Berg, "Correction of non-uniform attuentaion in cardiac SPECT imaging," *J. Nuc. Med.*, Vol. 30, pp. 497–507, 1989.

30. J.A. Sorenson, "Quantitative measurement of radioactivity in vivo by whole body counting," *Instrum. Nucl. Med.*, Vol. 2, pp. 311–347, 1974.

31. A.V. Bronnikov, "Reconstruction of attenuation map using discrete consistency conditions," *IEEE Trans. Med. Imaging*, Vol. 19, pp. 451–462, 2000.

32. A. Welch, R. Clack, F. Natterer, and G. Gullberg, "Toward accurate attenuation correction in SPECT without transmission measurements," *IEEE Trans. Med. Imaging*, Vol. 16, pp. 532–541, 1997.

33. M.V. Ranganath, A.P. Dhawan, and N. Mullani, "A multigrid expectation maximization reconstruction algorithm for positron emission tomography," *IEEE Trans. Med. Imaging*, Vol. 7, pp. 273–278, 1988.

34. A. Raheja and A.P. Dhawan, "Wavelet based multiresolution expectation maximization reconstruction algorithm for emission tomography," *Comput. Med. Imaging Graph.*, Vol. 24, pp. 87–98, 2000.

35. S.K. Mitra and J.F. Kasier (Eds), *Handbook of Digital Signal Processing*, John Wiley and Sons, Inc., 1993.

36. A.P. Pentland, "Interpolation using wavelet bases," *IEEE Trans. Pattern Anal. Mach. Intell.*, Vol. 16, No. 4, pp. 410–414, 1994.

37. M.-H. Yaou and W.-T. Chang, "Fast surface interpolation using multiresolution wavelet transform," *IEEE Trans. Pattern Anal. Mach. Intell.*, Vol. 16, No. 7, pp. 673–688, 1994.

38. C.K. Chui, "On compactly supported spline wavelets and a duality priciple," *Trans. Am. Math. Soc.*, Vol. 330, No. 2, pp. 903–915, 1992.

39. A. Cohen, I. Daubechies, and J.-C. Feauveau, "Biorthogonal bases of compactly supported wavelets," *Comm. Pure Appl. Math.*, Vol. 45, No. 5, pp. 485–560, 1992.

40. S. Ogawa, D.W. Tank, R. Menon, J.M. Eillermann, S.G. Kim, H. Merkle, and K. Ugurbil, "Intrinsic signal changes accompanying sensory simulation," *Proc. Nat. Acad. Sci. USA*, Vol. 89, pp. 5951–5955, 1992.

41. M.S. Cohen and S.Y. Bookheimer, "Localization of brain function using MRI," *Trends Neurosci.*, Vol. 17, pp. 208–276, 1994.

42. V. Solo, P. Purdon, R. Weisskoff, and E. Brown, "A signal estimation approach to functional MRI," *IEEE Trans. Med. Imaging*, Vol. 20, pp. 26–35, 2001.

43. T.B. Harshbarger and D.B. Tweig, "Iterative reconstruction of single-shot spiral MRI with off resonance," *IEEE Trans. Med. Imaging*, Vol. 18, pp. 196–205, 1999.

44. J.U. Quistguard, "Signal acquisition and processing in medical diagnostic ultrasound," *IEEE Signal Process. Mag.*, pp. 67–74, 1997.

45. M. Karaman, M.A. Kutay, and G. Bozdagi, "An adaptive speckle suppression filter for medical ultrasound imaging," *IEEE Trans. Med. Imaging*, Vol. 14, pp. 283–292, 1995.

46. X. Hao, S. Gao, and X. Gao, "A novel multiscale nonlinear thesholding method for ultrasonic speckle suppressing," *IEEE Trans. Med. Imaging*, Vol. 18, pp. 787–794, 1999.

47. T.R. Nelson, D.B. Downey, D.H. Pretorius, and A. Fenster, *Three-Dimensional Ultrasound*, Lippincott Williams and Wilkins, Philadelphia, 1999.

48. E.O. Ofili and N.C. Nanda, "Three-dimensional and four-dimensional echocardiography," *Ultrasound Med. Biol.*, Vol. 20, pp. 669–675, 1994.

49. H.N. Cardinal, J.D. Gill, and A. Fenster, "Analysis of geometrical distortion and statistical variance in length, area and volume in a linearly scanned ultrasound image," *IEEE Trans. Med. Imaging*, Vol. 19, pp. 632–651, 2000.